Received 27 February 2023; revised 19 April 2023; accepted 2 May 2023.
Date of publication 9 May 2023; date of current version 30 May 2023.

Digital Object Identifier 10.1109/OJUFFC.2023.3274512

Microbubble Identification Based on Decision Theory for Ultrasound Localization Microscopy

ALEXANDRE CORAZZA, PAULINE MULEKI-SEYA, ADRIAN BASARAB, AND BARBARA NICOLAS

Univ Lyon, INSA-Lyon, Université Claude Bernard Lyon 1, UJM-Saint Etienne, CNRS, Inserm, CREATIS UMR 5220, U1294, F-69100 Villeurbanne, France

Corresponding author: A. CORAZZA (Alexandre.corazza@creatis.insa-lyon.fr)

This work was supported in part by LABEX CELYA under Grant ANR-10-LABX-0060, in part by LABEX PRIMES under Grant ANR-11-LABX-0063 both through Université de Lyon within the Program "Investissements d'Avenir" operated by the French National Research Agency (ANR) under Grant ANR-11-IDEX-0007, and in part by the France Life Imaging TRAIL Project ANR-11-INBS-0006.

ABSTRACT Ultrasound localization microscopy (ULM) enables the evaluation of the vascular microstructure by detecting, localizing, and tracking microbubbles (MBs) in the vascular network. ULM provides a vascular map of the network with improved spatial resolution but with an acquisition time of several minutes. Thus, it is of great importance to increase the number of MBs detected in order to limit the acquisition time. The standard MB detection method in ULM assumes that the contrast agents are the highest-intensity structures on the ultrasound images. However, *in vivo* data show that MB intensity may be lower than residual tissue or even noise. Thus, to facilitate the detection of these MBs, an MB detector based on decision theory is proposed in this paper. In this study, the proposed method based on the Neyman–Pearson criterion is compared with the standard intensity-based and the normalized cross-correlation detection methods on simulated and *in vivo* rat brain and kidney data. The new detection method makes it possible to control the false positive detection rate without degrading the MB detection rate on simulated data, to enhance the ULM vessel map resolution on *in vivo* brain data and to detect more vessels on *in vivo* kidney data.

INDEX TERMS Ultrasound localization microscopy, microbubble detection, decision theory, Neyman–Pearson criterion, constant false alarm rate detection.

I. INTRODUCTION

Ultrasound localization microscopy (ULM) is a noninvasive method for characterizing the vascular microstructure with a resolution beyond the diffraction limit. This technique may offer a better understanding of brain diseases such as Alzheimer's or Parkinson's [1]. It can also help to detect tumor angiogenesis [2], [3], recognizable by its tortuous microvasculature structure [4] with slow and irregular blood flow [5], [6], to characterize tumors [7], and to assess anticancer therapy response [7], [8].

The first step in ULM consists in injecting microbubble (MB) ultrasound contrast agents into the vascular network and acquiring radiofrequency (RF) signals for several minutes. These RF data are beamformed with the delay-and-sum (DAS) method [9] to obtain ultrasound images (Fig. 1a). Then, a signal-processing chain is applied on these images to remove biological tissues and to detect, localize precisely, and track MBs through time in order to accumulate all their trajectories and retrieve the vascular map with a micrometer resolution [10], [11]. A standard ULM algorithm from Performance Assessment of Localization Algorithm (PALA) toolbox is available online at https://github.com/AChavignon/PALA [12]. The different signal-processing steps of the classic ULM are described below and illustrated in Fig. 1b-f. Step (b) of the standard ULM algorithm from PALA consists in tissue filtering (Fig. 1b), *i.e.*, separating the tissue from the MBs. The most commonly used method is based on the singular value decomposition (SVD) of the Casorati matrix obtained from the sequence of ultrasound images [13]. The choice of the ideal number of singular values corresponding to tissue and noise to be removed can be defined by identifying the tissue,

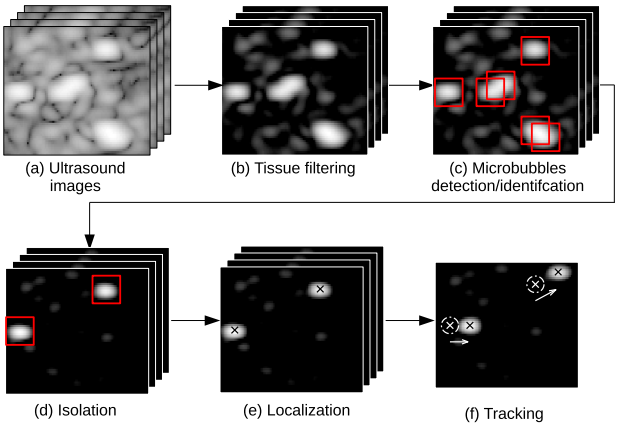

FIGURE 1. ULM signal-processing chain proposed in [11].

MBs, and noise areas in the distribution of singular values [14]. In step (c), MBs are detected on these filtered images (Fig. 1c). For this purpose, the standard method detects local maxima in each image and retains only a selected number of maxima with the highest intensities [10]. Regions of interest (ROIs) are built around these maxima with a size being defined according to the size of the point spread function (PSF). Other detection methods are presented in the literature, based on intensity threshold as in [15] and [16], which is equivalent to choosing a number N of maxima to be retained, with a threshold equal to the value of the N^{th} maxima. The detection method can also be based on the PSF shape as in [17] and [18], where a normalized cross-correlation (NCC) is performed with an estimated PSF or a Gaussian kernel. In the isolation step (Fig. 1d), only ROIs with not more than N_{LM} MB, a parameter chosen by the user, are retained to decrease the bias of the localization algorithm [10]. The localization step (Fig. 1e) is a very important stage of the ULM chain since it offers micrometer resolution, below the diffraction limit [19], [20]. Considering the selected ROI from the previous step, the algorithm localizes with sub-wavelength precision the center of MBs in each ROI. Several localization algorithms were developed for ULM, based on the hyperbola summit in the RF signals [21] or on ultrasound image interpolation [22], Gaussian fitting with the PSF [18], weight average [23], or radial symmetry [24]. Finally, the algorithm provides a list of MBs positions. The aim of the tracking step (Fig. 1f) is to pair positions at time t with those at time $t - 1$ in order to follow the trajectory of each MB. The fastest solution for this is to pair the MBs using the nearest-neighbor method as in [25]. Another method is the Hungarian pairing algorithm [26] that minimizes the sum of distances between each possible pair. The tracking can also be based on Markov Chain Monte Carlo approaches by modeling the MBs appearance and persistence with probability laws and by maximizing the likelihood of the tracks regarding this model [16], [27]. The tracking step is also used as a filter to remove tracks that are not long enough in time [10].

The microvascular map is finally obtained by accumulating all trajectories to create a density map. A velocity map can be computed using the difference in bubble position between two frames.

One of the well-known challenges in ULM is to draw the most complete map in minimum acquisition time. Different strategies were evaluated to increase the number of detected MBs at different steps of the ULM. For example, the use of nonlinear ultrasound excitation as amplitude [28] or phase [29] modulation allows one to retain almost only MB signals. Brown and Hoyt [30] observed an average increase of 28.3%, and up to 52.6%, in the number of MBs detected using a pulse inversion strategy compared with a B-mode imaging strategy. In the filtering step, alternatives to SVD filtering were tested to avoid removing the slowest MBs, such as the robust principal component analysis (RPCA) that uses the sparsity of MBs in the images to filter tissues [31], [32]. In the isolation step, strategies to separate bubbles depending on their direction to limit their suppression were applied using a 3D conical filter [33]. For this, the ultrasound data have to be filtered in wave vector – temporal pulsation space [34] obtained by applying a 3D Fourier transform to the 2D space and time data. A final example of a strategy to improve the ULM map, without increasing the number of MBs detected, is achieved in the tracking step thanks to a Kalman model [35], [36]. The Kalman filter enables the filtering of tracks as a function of their direction. The principle is to use the past direction and speed of MBs to estimate their future position. If the measured position given by the localization and tracking algorithm is too far away from the prediction, it is corrected or removed. This improvement is an interesting denoising tool for removing random-looking trajectories in ULM images. Finally, some recent studies evaluated the potential of supervised deep learning in ULM. Given that the ground truth was not available in experimental setups, the training step was performed within these studies on simulated images of moving MBs [37]. Promising results have been shown, especially in the case of high MBs concentration [38], [39], [40], potentially interesting for reducing the acquisition time. However, the potential of deep learning for ULM was less explored for *in vivo* cases. It is thus still not clear if the synthetic training datasets are realistic enough to allow the network to generalize well to experimental data [37].

In this paper, an improvement of the MB detection step is proposed (Fig. 1c). As explained previously, the standard MB detection method is based on the intensity of MBs. However, from *in vivo* ultrasound images it has been noted that MB intensity may be lower than tissue or noise in certain conditions. One can assume, for example, that MBs in capillaries may present a lower intensity due to their limited range of oscillation. Moreover, the SVD filter attenuates (and even removes) the slowest MBs [41]. Consequently, these SVD-attenuated MBs are not detected by the algorithm. As the challenge of ULM is to image a maximum number of vessels in a minimum amount of time, it is very important to improve the MB detection rate, especially in capillaries where the passage of bubbles is not frequent.

To deal with this challenge, a detection method based on decision-theory tools, known as a Constant False Alarm Rate (CFAR) detection method in RADAR applications [42], [43], is proposed in this work. The remainder of the paper is structured as follows. First, the standard detection methods of the literature are presented, then the problem of MB detection is modeled using decision theory concepts and the resulting solution based on the Neyman–Pearson criterion is explained. Second, the ultrasound data used to validate the proposed approach are described. Finally, the decision theory-based detection is compared with the intensity-based and normalized cross-correlation algorithms on simulated and *in vivo* ultrasound images of rat brain and kidney.

II. STATE OF THE ART OF MICROBUBBLE IDENTIFICATION METHODS

A. INTENSITY-BASED METHOD

Intensity-based detection assumes that the MBs are corresponding to the highest intensity local maxima in the ultrasound images $I(t)$ [15], [16]. The detection of these particular local maxima can be achieved by two similar techniques. An intensity threshold T can be set and all local maxima with values higher than T are considered as potential MBs. Thus, the filtered images $C_{int}(t)$ containing only the supposed MBs are given by:

$$C_{int}(t) = I(t)\,[I(t) \geq T], \tag{1}$$

where $[\cdot]$ is a binary variable equal to 1 if the condition $\cdot$ is verified, and 0 otherwise. The second approach sets a number $N_{bubbles}$ of potential MB to be detected in each image $I(t)$ [10]. In this case, the threshold T is equal to the $N^{th}_{bubbles}$ local maximum intensity. Both techniques have advantages and drawbacks. On one hand, the first approach does not consider the fact that the SNR may vary in time due to movements. On the other hand, the second approach is also limited as the number of MBs varies in time. However, mostly due to the tracking filtering, the two approach provide equivalent results in most practical situations.

B. NORMALIZED CROSS-CORRELATION-BASED METHOD

With the main objective of obtaining a MB detection robust to intensity variations, NCC-based methods exploit the similarity of a PSF model K with the structures in an ultrasound image I. The NCC coefficient γ_{NCC}, corresponding to the similarity of the PSF model with a local image patch centered on the pixel (i, j), is given for each (i, j) by:

$$\gamma_{NCC}(i,j) = \frac{\sum_{x,z}(I(x,z) - \mu_I)(K_{i,j}(x,z) - \mu_K)}{\sqrt{\sum_{x,z}(I(x,z) - \mu_I)^2 \sum_{x,z}(K_{i,j}(x,z) - \mu_K)^2}} \tag{2}$$

Within the summations, the lateral and axial indexes (x, z) ranges depend on (i, j) and on the size of the kernel S_K: $(x, z) \in [i-\frac{S_K}{2}, i+\frac{S_K}{2}]\times[j-\frac{S_K}{2}, j+\frac{S_K}{2}]$. The kernel K is noted as $K_{i,j}(x, z) = K(x - i, z - j)$. The variable μ_I corresponds to the mean value of the sample extracted from the image I centered on pixel (i, j) with a size S_K, and μ_K is the PSF model mean value. This cross-correlation coefficient is less sensitive to the image intensity thanks to the normalization by the mean and the standard deviation values. The filtered images $C_{NCC}(t)$ containing the potential MBs are computed as follows:

$$C_{NCC}(t) = \gamma_{NCC}\,[\gamma_{NCC} \geq \tau_{NCC}], \tag{3}$$

with τ_{NCC} corresponding to the constraining threshold concerning the similarity between the PSF model and the local image patches. For low values of τ_{NCC}, the MB selection in (3) is more tolerant regarding the PSF shape but with a risk of undesired detections. This threshold is usually chosen at 0.6 [18] but it can be set at a lower value as 0.4 to estimate correctly the velocity in the case of bolus injection [17]. Concerning the PSF model, it can be considered as a Gaussian kernel [18], or estimated by simulating a PSF with an ultrasound simulation toolbox such as SIMUS [44] as in [17]. It can also be estimated experimentally by imaging a wire cross section [45].

III. PROPOSED DETECTION METHOD

A. MODEL

A method based on decision theory [46] is proposed in this work to improve the detection of MBs and is presented schematically in Fig. 1c. Let us denote by $x_{i,j}(t)$ the temporal signal corresponding to pixel location (i, j) extracted from a temporal ultrasound image sequence. Some examples of such temporal signals, for different spatial locations in Fig. 2a, extracted from an ultrasound image sequence of rat brain acquired *in vivo* (see Section IV for more details on these data), are plotted in Fig. 2b. The examples represent different situations: the signals corresponding to circle-, triangle-, and cross-marked pixels are extracted from vessels where MBs with different intensities are passing; the signal corresponding to the pixel marked by a square is extracted from a region with no vessel (i.e., with no MBs passing through it), thus representing the temporal speckle signature generated by tissue movement and electronic noise. One may note that the first three signals (circle-, triangle-, and cross-marked pixels) contain visible peaks that correspond to MBs. However, the amplitude of these peaks reported to the level of noise depends on the MB intensity. Therefore, MB detection from these signals may be challenging, in particular for low-intensity MBs (see, e.g., triangle- and cross-marked pixel examples) where a simple local maxima-based detection would fail.

Figure 2c presents the histograms of the four signals, illustrating the statistical distribution of such temporal signals. Observing the statistical behaviors of the temporal signals extracted from an ultrasound image sequence, a statistical model is derived including the following realistic assumptions: i) the noise is assumed to be Gaussian distributed, and ii) MB responses (peaks) are assumed to be constant for a given pixel but spatially variant, i.e., there may be differences from one pixel to another.

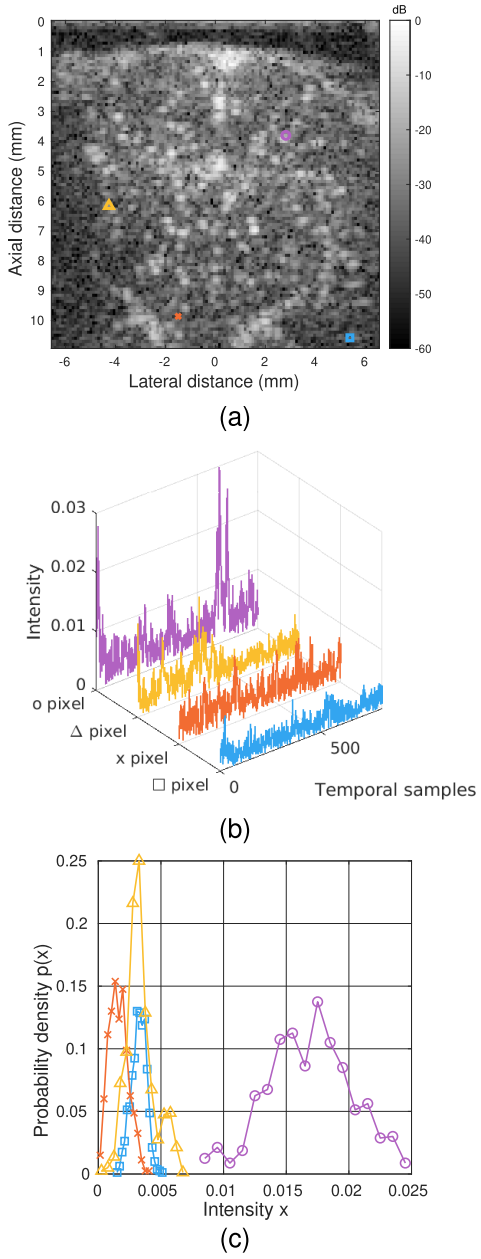

FIGURE 2. (a) Example of a rat brain ultrasound image from the PALA toolbox [12] shown with a 60-dB dynamic scale from which are extracted (b) four temporal signals corresponding to marked pixels in (a). (c) The histograms of these four temporal signals are shown. The circle, triangle, and cross markers are on pixels where MBs are passing, respectively, with high, medium, and low intensity compared to the noise level. On the cross pixel marker, no MB is passing.

Let us consider the following classic hypothesis:

H_0: the pixel value corresponds to noise only;

H_1: the pixel value corresponds to noise and to the passage of an MB.

Under these hypotheses, the value of (i, j) pixel at time t, i.e., $x_{i,j}(t)$, can be modeled as:

$$x_{i,j}(t) = \begin{cases} (x_{i,j}|H_0)(t) = T_{i,j}(t) \\ (x_{i,j}|H_1)(t) = B_{i,j} + T_{i,j}(t), \end{cases} \tag{4}$$

where $T_{i,j}(t)$ is a Gaussian random variable of mean $m_{i,j}$ and variance $\sigma^2_{i,j}$ modeling the signal generated by tissue motion and electronic noise. $B_{i,j}$ represents a constant value modeling the presence of an MB. It is important to underline that the statistics of the noise (mean and variance) and the intensity of the MB signal ($B_{i,j}$) are defined pixel-wise, which means that they may be different from one pixel to another. This choice has been made because not all MBs have the same intensity, and all the image regions are not affected by the same level of speckle.

Based on this signal model, the problem of bubble detection at time t and spatial position (i, j) is equivalent to deciding whether the signal $x_{i,j}(t)$ fulfils the H_0 or H_1 hypothesis. In this work, the decision rule considered is based on the following criteria [46]:

$$\Lambda(x_{i,j}) \triangleq \frac{p(x_{i,j}|H_1)}{p(x_{i,j}|H_0)} \underset{H_0}{\overset{H_1}{\gtrless}} \gamma_{i,j}, \tag{5}$$

where Λ is the likelihood ratio, $p(X)$ corresponds to the probability density function of the random variable X, and $\gamma_{i,j}$ is a pixel-wise threshold. The symbol $\underset{H_0}{\overset{H_1}{\gtrless}}$ stands for the classic decision hypothesis, i.e., H_1 if $\Lambda(x_{i,j}) > \gamma_{i,j}$, and H_0 otherwise. In the next subsections, the likelihood ratio is expressed based on the statistical assumptions explained above, and several approaches to define the threshold are provided. Note that the pixel subscripts i, j and time t are omitted in the following for the sake of clarity. In other words, the theoretical developments are applied for one spatio-temporal pixel location.

B. LIKELIHOOD RATIO $\Lambda(x)$

Based on the statistical model in (4), the probability density ratio $\Lambda(x)$ is simply expressed by the ratio of two Gaussian functions with the same variance but different mean values:

$$\Lambda(x) = \frac{p(x|H_1)}{p(x|H_0)} = \frac{\frac{1}{\sigma\sqrt{2\pi}} e^{-\frac{1}{2}\frac{(x-(m+B))^2}{\sigma^2}}}{\frac{1}{\sigma\sqrt{2\pi}} e^{-\frac{1}{2}\frac{(x-m)^2}{\sigma^2}}}. \tag{6}$$

After simplification and by taking the logarithm of $\Lambda(x)$, one obtains

$$ln(\Lambda(x)) = \frac{1}{2\sigma^2} B(2x - 2m - B). \tag{7}$$

By re-injecting the previous expression into (5), the decision rule becomes

$$x \underset{H_0}{\overset{H_1}{\gtrless}} \frac{\sigma^2}{B} \ln(\gamma) + m + \frac{B}{2} \triangleq \eta. \tag{8}$$

The decision regarding hypothesis H_0 or H_1 is thus conditioned by the value of the pixel compared with a threshold η that depends on the statistical distribution of speckle noise (its mean m and variance σ^2), on the MB intensity B, and on the threshold γ. All these parameters are unknown in practical situations, and should thus be estimated from the data or preset to fixed values. In particular, the value of γ can

be fixed based on several decision theory approaches such as Bayes [47], MiniMax [47], or Neyman–Pearson [46] criteria. The MB detection algorithm introduced in this work uses the latter, sustained by its accuracy and robustness and by the fact that it does not require any *a priori* information about the probability of detecting an MB, unlike the Bayes criterion.

C. THRESHOLD ESTIMATION BY THE NEYMAN–PEARSON CRITERION

The principle of the Neyman–Pearson (NP) method is to estimate the threshold η from the false-alarm rate α_0, which has to be pre-defined respecting the application constraints. In our case, α_0 is related to the risk of false detection of an MB in a given pixel. The influence of its value on the final results will be discussed in the Results section. By definition, α_0 is given by

$$\alpha_0 \triangleq \int_{\eta}^{+\infty} p(x|H_0)\mathrm{d}x. \tag{9}$$

By incorporating the statistical model x under hypothesis H_0 in (4) into (9), one obtains:

$$\alpha_0 = \int_{\eta}^{+\infty} \frac{1}{\sigma\sqrt{2\pi}} e^{-\frac{1}{2}\frac{(x-m)^2}{\sigma^2}} \mathrm{d}x. \tag{10}$$

Following a variable change $u = \frac{x-m}{\sigma\sqrt{2}}$, (9) becomes:

$$\alpha_0 = \frac{1}{\sqrt{\pi}} \int_{\frac{\eta-m}{\sigma\sqrt{2}}}^{+\infty} e^{-u^2}\mathrm{d}u, \tag{11}$$

and finally, using the complementary error function (1-erf(·)):

$$\alpha_0 = \frac{1}{2}(1 - \mathrm{erf}(\frac{\eta - m}{\sigma\sqrt{2}})). \tag{12}$$

with erf(·) the error function defined as:

$$\mathrm{erf}(X) = \frac{2}{\sqrt{\pi}} \int_0^X e^{-u^2}\mathrm{d}u \tag{13}$$

η can be isolated from (12) thanks to the inverse error function $\mathrm{erf}^{-1}(\cdot)$ and can be replaced in (8) in order to express $\ln(\gamma)$ as a function of α_0, m and σ as follows:

$$\ln(\gamma) = \frac{B}{\sigma^2}(\sigma\sqrt{2}\,\mathrm{erf}^{-1}(1-2\alpha_0) - \frac{B}{2}). \tag{14}$$

Using the results from (14) in (8), the decision rule of MB detection becomes

$$x \underset{H_0}{\overset{H_1}{\gtrless}} \sigma\sqrt{2}\,\mathrm{erf}^{-1}(1-2\alpha_0) + m \triangleq \eta. \tag{15}$$

The decision criterion in (15) can be easily interpreted based on the choice of the value of α_0. Given that erf^{-1} is an increasing function, a low false-alarm rate α_0 induces a high threshold η, which narrows the region of the hypothesis H_1, i.e., of MB detection. Consequently, the probability of detecting MBs in tissues, i.e., outside the vessels, is reduced. It is also worth noting that the threshold η depends on the speckle temporal variance, which robustifies it compared with, e.g., the MiniMax criterion. The two approaches are equivalent for $\alpha_0 = 0.5$. Moreover, for $\alpha_0 = 1$, the threshold is equal to $m - 2\sqrt{2}\sigma$, which, for a Gaussian distribution, means that more than 99.73% of the pixels values are classified as H_1, corresponding to MB detection. Of course, such a high detection rate is not relevant in ULM. On the contrary, for $\alpha_0 = 0$, only 0.27% of the pixels values would be classified as H_1, which would represent a high risk of missing most of the MBs in ULM. The influence of α_0 in ULM will be discussed in the Results section, restricting it to the interval]0, 0.5[that corresponds to plausible MB detection rates in ULM.

D. ESTIMATION OF NOISE STATISTICAL MOMENTS

For the NP criterion, the pixel-wise threshold η depends on the statistical moments of the noise, *i.e.*, the mean m and the standard deviation σ. To estimate these parameters, one can assume that MB passage is rare and compute empirically the noise mean and standard deviation using the whole signal. However, for a high concentration of bubbles, the bias of such an empirical estimation may be too high. Consequently, a robust estimator, *i.e.*, non-sensitive to outliers, is more suitable for our application. A well-known robust estimator for the noise mean is the median and for the noise standard deviation, the median absolute deviation (MAD). Note that both median and MAD are computed in the temporal dimension. The MAD for the pixel (i, j) is defined as [48]:

$$\mathrm{MAD}_{i,j} = \mathit{median}(|x_{i,j}(t) - \mathit{median}(x_{i,j}(t))|). \tag{16}$$

For a Gaussian distribution, the standard deviation can be deduced by:

$$\sigma = \frac{1}{\sqrt{2}\mathrm{erf}^{-1}(\frac{1}{2})}\mathrm{MAD}. \tag{17}$$

E. DETECTION MAPS

Coming back to the whole set of data, the NP criterion described above is applied to each temporal sample $x_{i,j}(t)$ of the pixel (i, j). It is then possible to build a block of detection maps C as follows:

$$C_{i,j}(t) = (x_{i,j}(t) - \eta_{i,j})\,[x_{i,j}(t) \geq \eta_{i,j}], \tag{18}$$

where $[\cdot]$ is a binary variable equal to 1 if the condition $\cdot$ is verified, and 0 otherwise. The term $(x_{i,j}(t) - \eta_{i,j})$ provides information on the relevance of the detection.

F. INTEGRATION OF THE DECISION MAP IN ULM FRAMEWORK

The NP decision criterion is used to improve the detection step of ULM. The NP criterion is first applied on the beamformed images after SVD filtering, resulting in the detection maps $C_{i,j}(t)$ in (18). Local maxima are then detected on these maps. Rectangular ROIs are defined around the retained maxima, used as input for the localization step. The final pseudocode is given in Algorithm 1, which takes as input the original (without any filtering) beamformed ultrasound image sequence denoted by $\mathbf{I}(i, j, t)$.

Algorithm 1 ULM Algorithm Using the Proposed NP-Based MB Detection

Input: Native ultrasound image sequence $\mathbf{I}(i, j, t)$ of size $[N_i, N_j, N_t]$

Tissue and noise filtering by SVD
$\mathbf{X}(i, j, t) = SVD(\mathbf{I}(i, j, t))$
Microbubble detection
Loop over each spatial pixel
for $i = 1$ *to* N_i **do**
  for $j = 1$ *to* N_j **do**
    Estimate noise mean $m_{i,j}$ by computing the median value of $x_{i,j}(t)$
    Estimate noise standard deviation $\sigma_{i,j}$ using (17)
    Compute the threshold $\eta_{i,j}$ using (15)
    Compute the maps $C_{i,j}(t)$ using (18)
Loop over each temporal frame
for $t = 1$ *to* N_t **do**
  Find the local maxima in $\mathbf{C}$(t)
  Build ROIs around the local maxima
  Isolation
  Remove ROIs with more than N_{LM} local maxima
  for *each ROI* **do**
    Subwavelength localization
    Apply localization method to each image $\mathbf{X}(t)$ in the boundaries defined by previous ROIs
Tracking Pair MB locations at times t and $t-1$
Mapping Accumulate tracks or compute MB velocity
Output: Accumulated tracks and MB velocity maps

IV. RESULTS AND DISCUSSIONS

A. SIMULATED AND IN VIVO DATA

MB detection methods are evaluated through three datasets available online at https://zenodo.org/record/4343435 from the PALA toolbox, which provides a benchmark for evaluating the ULM algorithm [12]. The simulated dataset (named PALA_data_InSilicoFlow) was composed of 20,000 simulated ultrasound images of moving MBs at various constant velocities in crossing vessels of different sizes and shapes [12]. A moving residual speckle and residual bright slow tissue component has been added on the images to increase the realism of the simulations [49]. The residual bright slow tissue component may correspond to traces of specular reflections from an interface not completely removed with the SVD. These simulated images are supposed to be images after tissue filtering in order to control the SNR level and thus evaluate the influence of the residual speckle level. To simulate the residual speckle, a uniform random 3D matrix $[N_i, N_j, N_t]$ in size has been generated and convolved in space and time directions by Gaussian kernels. The kernel variance in the space direction defines the speckle pattern width and the variance in the time direction defines the movement amplitude. In this simulation, both variances

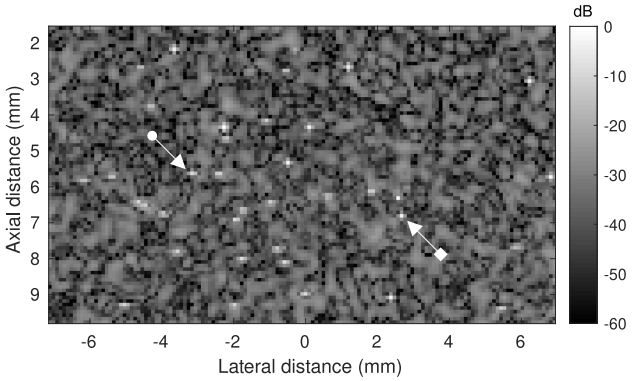

FIGURE 3. Simulated ultrasound image with microbubbles from the PALA toolbox [12] with moving speckle and bright tissue addition. An example of a microbubble is indicated by the arrow with a circle and a residual ponctual bright tissue is indicated by the arrow with a square.

were empirically set to 1 wavelength denoted by λ. The 3D matrix amplitude was then normalized by its maximum and finally multiplied by the chosen SNR. The bright residual tissue is simulated by 10 additional slow-moving bright Dirac scatterers at random coordinates convolved with a Gaussian kernel of Gaussian random variance with a mean of 0.5λ and a variance of 0.1λ to simulate the PSF width variations. Their intensity means are two times the maximum intensity of all images and their standard deviations are equal to 1% of the mean. Their movements are cyclic, induced by an alteration of the scatterer coordinates, mimicking a breathing movement. This movement is simulated by a linear translation with a velocity of $1/250$ λ/image in the lateral and axial axes. The cyclic behavior is ensured by concatenating the movement vector with its flip. This design of bright residual tissue is extremely simplified and does not correspond visually with what could be seen on ultrasound images. Nonetheless, it allows us to evaluate the effect of bright residual tissue on the detection methods. The results can be seen in Fig. 3, where the MBs are scatterers with relatively large PSF, the residual bright tissues are the brightest pixels, and the granite pattern is the residual speckle.

The second dataset (named PALA_data_InVivoRat BrainBolus) was composed of 213 blocks of 800 beamformed images of *in vivo* rat brain measurements with two bolus injections of MBs, which corresponds to an acquisition time of 171 s. In this study, only the data with the first bolus injection are used, *i.e.*, the first 85.6 s of acquisition. This dataset is interesting for validating the NP detection since it contains MBs brighter than others for each given image, as can be seen in Fig. 4. It is used to analyze the NP detection in high (at the beginning of the bolus injection) and low MB (at the end of the bolus injection) concentration. A high MB concentration enables the evaluation of the robustness of the noise statistical moments estimator.

The last dataset (PALA_data_InVivoRatKidney) was composed of 238 blocks of 790 beamformed images of *in vivo* rat kidney with a bolus injection, which corresponds to 185 s of

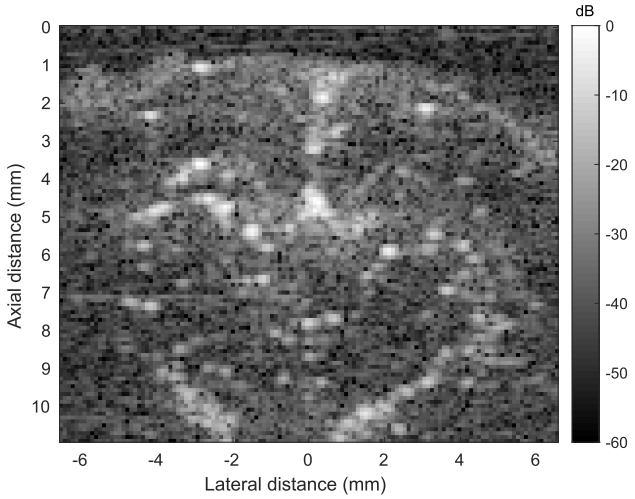

FIGURE 4. Example of rat brain ultrasound image with microbubbles, from the PALA toolbox [12].

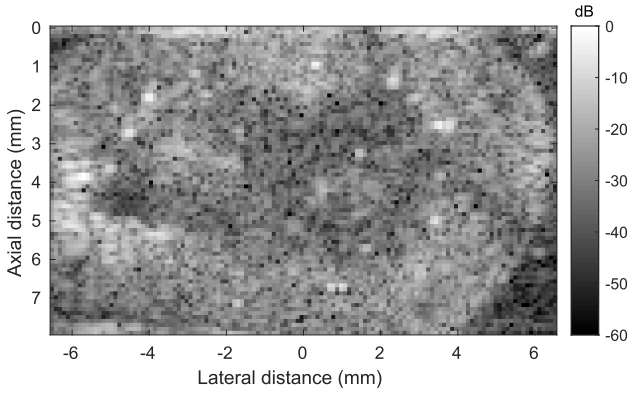

FIGURE 5. Example of rat kidney ultrasound image with microbubbles, from the PALA toolbox [12].

TABLE 1. Simulation and acquisition parameters for each dataset [12].

Parameter	Simulation	Rat brain	Rat kidney
Ultrasound frequency	15MHz	15MHz	15MHz
Number of tilted plane wave	3	3	5
Pixel size	λ	λ	λ
Frame rate	500Hz	1000Hz	1000Hz
Acquisition time	40s	85.6s	92.8s

acquisition. In order to compare the results with the rat brain example in term of acquisition time, only the first 92.8 s of the acquisition are used in this study. An example is given in Fig. 5; as can be seen, some MBs are moving in a low SNR area and thus it will be interesting to evaluate the results in such a context. The main acquisition parameters of all the datasets presented here are given in Tab. 1.

B. COMPARISON METHOD AND HYPER-PARAMETER CHOICE

Table 2 summarizes the most important hyper-parameter and its signification, of the proposed methods and the techniques used for comparison.

TABLE 2. Main hyper-parameter of each evaluated detection method.

Method	Hyper-parameter	Signification
Intensity-based	$N_{bubbles}$	number of local maxima to consider as potential MBs per image
NCC	τ_{NCC}	minimum correlation value for which the structures are considered as MBs
NP	α_0	false alarm rate, definition given in (15)

TABLE 3. ULM parameters for each dataset. the first four parameters are specific to the detection methods and the last ones are common to all methods.

Parameter	Simulation	Rat brain	Rat kidney
$N_{bubbles}$	40	50 to 300	100 and 200
τ_{NCC}	0.6 and 0.7	0.6 to 0.8	0.6 and 0.7
NCC Kernel	Estimated PSF	Gaussian	Gaussian
α_0	10^{-5}% to 10%	10^{-5}% to 1%	10^{-5}% to 0.1%
SVD cutoff	No SVD	10	10
MaxDist	2λ	2λ	1.5λ
MinLength	15 frames	10 frames	15 frames
N_{LM}	1	4	3

For NCC-based method, the kernel choice is a key-point to provide correct results. For the simulation study, the PSF shape and size were estimated by selecting a PSF from a simulated ultrasound image of the dataset without noise. For the *in vivo* study, the extraction of a PSF directly from an image was not possible because of the noise, so the PSF was modeled as a Gaussian with a standard deviation chosen by analyzing the intensity drop between the main lobe and side lobes on experimental PSF examples. Thus, the retained standard deviation for the brain and the kidney datasets was 1.75λ. The kernel size S_K presents a trade-off since a too wide window will risk to take information from neighboring PSF and a too narrow one may lack information about the PSF shape. The PSF size was empirically fixed at 5λ, for both *in vivo* studies, in order to ensure the best possible results. Then, to ensure a reliable reference, the ULM parameters in Tab. 3 are the same as those provided in the PALA toolbox script example. The main ULM parameters are:

- SVD cutoff: number of singular values removed,
- MaxDist: maximum linking distance between two localized MBs to enable pairing in the tracking step,
- MinLength: minimum length of track,
- N_{LM}: number of local maxima allowed in an ROI.

The localization algorithm used in this study was based on the radial symmetry due to its good performance/computational load compromise. For tracking, the Hungarian algorithm was used for the same reason and for its good performance within high frame rate acquisitions.

C. RESULTS FROM SIMULATED DATA

By applying the NP detection to the first dataset, the η thresholds of Eq. (15) are computed for each pixel (i, j) (called $\eta_{i,j}$),

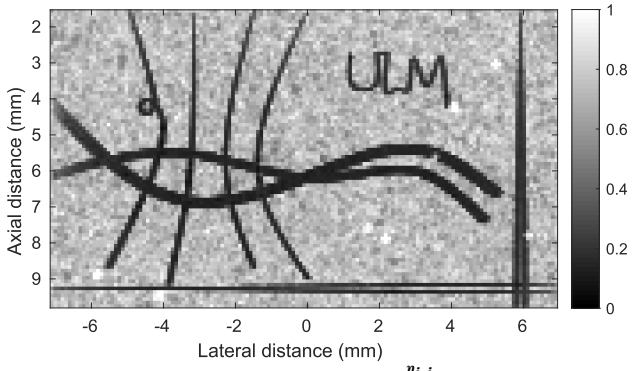

FIGURE 6. Normalized threshold map $\frac{\eta_{i,j}}{max(x_{i,j}(t))}$ of simulated data with the Neyman–Pearson method, $\alpha_0 = 0.1\%$.

which gives the normalized threshold map $\frac{\eta_{i,j}}{max(x_{i,j}(t))}$ in Fig. 6. For this example, a false-alarm rate α_0 of 1% is chosen. When the signal is higher than this threshold, an MB is detected. As the threshold is low in the vessel area it will ease MB detection. On the contrary, outside the vessels, the normalized threshold is close to 1. In that case, there is a low probability of detecting any MB at any time.

In order to evaluate and compare the intensity-based, the NCC and NP detection methods, standard detection metrics are used. A true positive (TP) is counted if an MB is detected and localized at a maximum range of $\lambda/4$ away from a real MB as per the ground truth, as done in [12]. A false positive (FP) is a detected MB without a simulated MB at a range of $\lambda/4$. Finally, a false negative (FN) is a missed detection and is counted if there is no detected MB at a range of $\lambda/4$ from a known MB position. This counting is performed after the tracking step by the function *PALA_PairingAlgorithm* of the PALA toolbox. The metrics are presented in Fig. 7 as a function of the SNR for the standard detection and for the NP detection with several values of α_0 in the simulated data. The TPs are represented in Fig. 7a, which shows the similarities between the methods except for NP with the low false-alarm risk α_0 of $10^{-5}\%$ and for the NCC with $\tau_{NCC} = 0.7$ that present a slightly lower number of TPs at a low SNR. However, this low false-alarm rate makes it possible to limit the FPs at low SNR, as can be seen in Fig. 7b for NP. Moreover, at any value of α_0, the NP method detects fewer FPs than the intensity-based detection method, since the latter is sensitive to the presence of bright residual tissue and detects it as an MB. The effect of the α_0 parameter is only measurable through FP detections because a low false-alarm rate limits them. For the NCC, the FP detections are more frequent than for NP with a low α_0 and they decrease while τ_{NCC} increases, which is consistent since a high τ_{NCC} is more restrictive. Note that the FP detections increase with the SNR, which is non-intuitive but is explained by the more frequent detection of bright residual tissue at high SNR. Finally, Fig. 7c shows that there is a difference in the FN metric only with the NCC method which misses more MBs. This can be explained by spatially-variance of the PSF. This is even more visible for *in vivo* studies where heterogeneity and phase aberration are not negligible. It can be concluded that the limitation of FP for the NCC method may be obtained at the price of a higher number of FN detections, and therefore a lower number of TP detections. Thus, the precisions ($TP/(TP + FP)$) of the NCC and NP detectors are better than the intensity-based method, particularly for a high τ_{NCC} and a low α_0. The sensitivity ($TP/(TP+FN)$) is lower only for the NCC method, particularly for a high τ_{NCC}. Note that since the localization was processed on the same images (see Algorithm 1, line 18), and given that 85% of the detected MBs coincide between the methods (this has been verified by pairing the MBs detected by the different methods with a maximum linking distance of 0.1λ), the localization performance was the same between the detection methods. Thus, these detection metrics are not biased by the localization.

D. RESULTS FROM IN VIVO RAT BRAIN DATA

The NP detection method is then applied to the *in vivo* dataset. The influence of α_0 on the threshold map $\eta_{i,j}$ is shown in Fig. 8. These maps are computed on 800 successive images as the acquisitions are continuous per block of 800 images. These 800 images enable the estimation of the noise statistical moments. It can be seen that the lower the false-alarm rate, the more constraining the threshold map. There is therefore a compromise between TP and FN detection. In the following results, the detection methods were applied to first bolus only, *i.e.*, to the first 107 blocks of 800 images.

The effect of each method hyperparameters is studied in Fig. 9. To begin, it is important to note that the ULM maps provided by the intensity and NCC-based methods have a large pixel value dynamics. Therefore, the scale of ULM images is usually compressed using a square or cubic root [12], to enhance the visualization of low intensity vessels. However, ULM maps built with the NP method have a smaller pixel value dynamic, better benefiting from a linear scale. For a fair comparison, in Fig. 9, it is not possible to display ULM maps with different scale compression methods. Thus, to avoid penalizing the comparison methods, ULM maps are compressed with a square root for all methods. Then, a histogram matching is applied to correct the scale of the ULM maps. This method has been initially developed to visually compare images without bias [50]. The histogram matching is performed by shifting the mean and adjusting the standard deviation of the pixels values: consider a reference image X and an image to correct Y. The image after histogram matching is determined by $I = aY + b$ with $a = \frac{\sigma_X}{\sigma_Y}$ and $b = \mu_Y - a\mu_X$, μ and σ corresponding to the mean and standard deviation of the corresponding images. The image in Fig. 9e has been chosen to be the reference image X since it has a dynamic in the average among the other images, so the adjustment effect of histogram matching does not affect excessively the images to correct. Note however that the histogram matching induces a loss of the physical meaning of the pixel values.

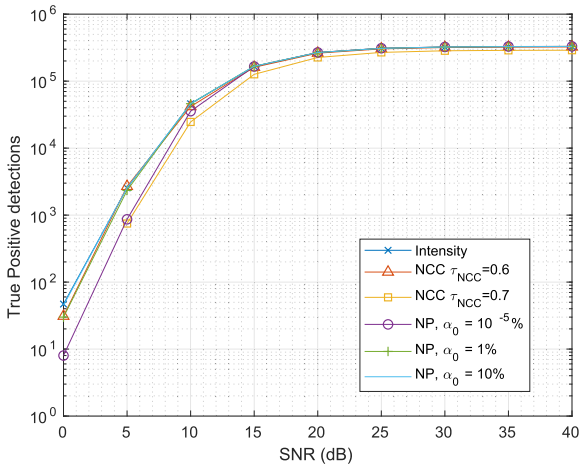

(a) True positive metric

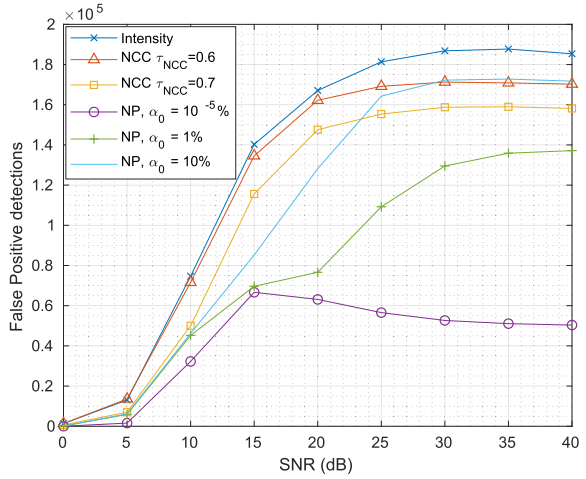

(b) False positive metric

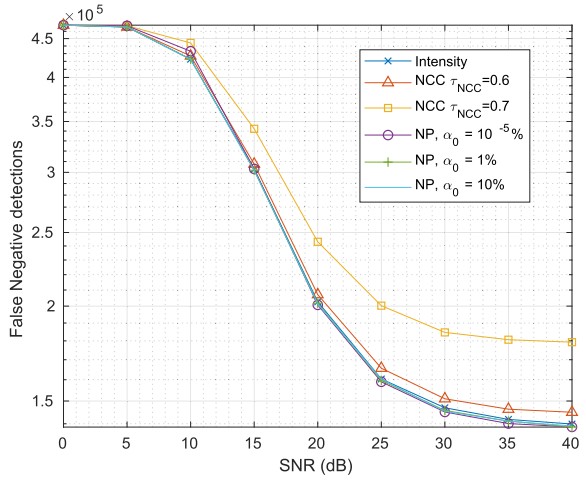

(c) False negative metric

FIGURE 7. Detection metrics for standard ULM and NP detection method with different false-alarm rate.

To simplify the visual comparisons, some areas are defined in Fig. 9a. The density maps of MBs for intensity-based

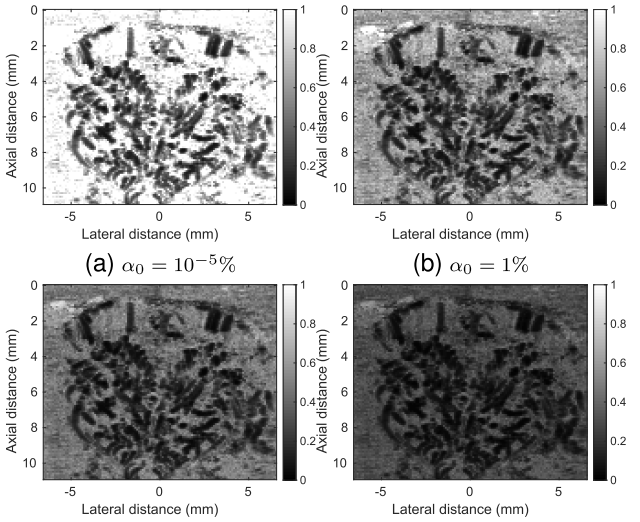

(a) $\alpha_0 = 10^{-5}\%$ (b) $\alpha_0 = 1\%$

(c) $\alpha_0 = 10\%$ (d) $\alpha_0 = 40\%$

FIGURE 8. Normalized threshold map $\frac{\eta_{i,j}}{max(x_{i,j}(t))}$ of rat brain data with the NP method, (a) $\alpha_0 = 10^{-5}\%$, (b) $\alpha_0 = 1\%$, (c) $\alpha_0 = 10\%$, (d) $\alpha_0 = 40\%$.

detection are presented in Fig. 9a, b, c for different $N_{bubbles}$ parameters. First of all, for the intensity-based method, the results for the empirically chosen $N_{bubbles}$ parameter proposed in the PALA toolbox script at 100 MBs is presented in Fig. 9b. If one is looking to remove artifacts in the area E, an idea would be to decrease the $N_{bubbles}$, *e.g.*, to 50 MBs as in Fig. 9a. However, this includes an erosion of some vessels (area C). On the other hand, if one's objective is to detect more vessels, the $N_{bubbles}$ parameter has to be increased, *e.g.*, to 300 MBs as in Fig. 9c. The cost of newly detected vessels (*e.g.* area C) with the intensity-based method is a higher number of artifacts (areas A and E) and a clear loss in resolution (*e.g.* in area B) which will be further studied hereafter in this paper. The proposed $N_{bubbles}$ parameter of 100 MBs can thus be considered as a good choice. The maps for the NCC detector are presented in Fig. 9d, e, f for different τ_{NCC} parameters. This parameter reflects the tolerance given to the similarity of the MBs in the image to the Gaussian PSF model. A too high τ_{NCC} parameter leads to false negative detections as represented in Fig. 9d where the major part of vessels are missed. For the chosen parameter τ_{NCC} at 0.7 in Fig. 9e, the NCC detector allows to recover a complete vessel map with less artefacts (area E) and a better resolution (area B) compared to Fig. 9b. However, some vessels are disconnected (areas A and D). One can try to decrease τ_{NCC} to 0.6 to make these vessels connected, but the vessels are still disconnected in area A and partially reconnected in area D but some false positive detections (area E) and artefacts occur (*e.g.* area A). This confirms the observations concerning the NCC in the simulation study: there is a compromise between the TP and the FP detections. With the NP detection, we propose a new parameter α_0 to control the false alarm rate.. The results for NP detection with different α_0 from $10^{-5}\%$ to 1% are presented in Fig. 9g, h, i. In Fig. 9g, for a very constraining

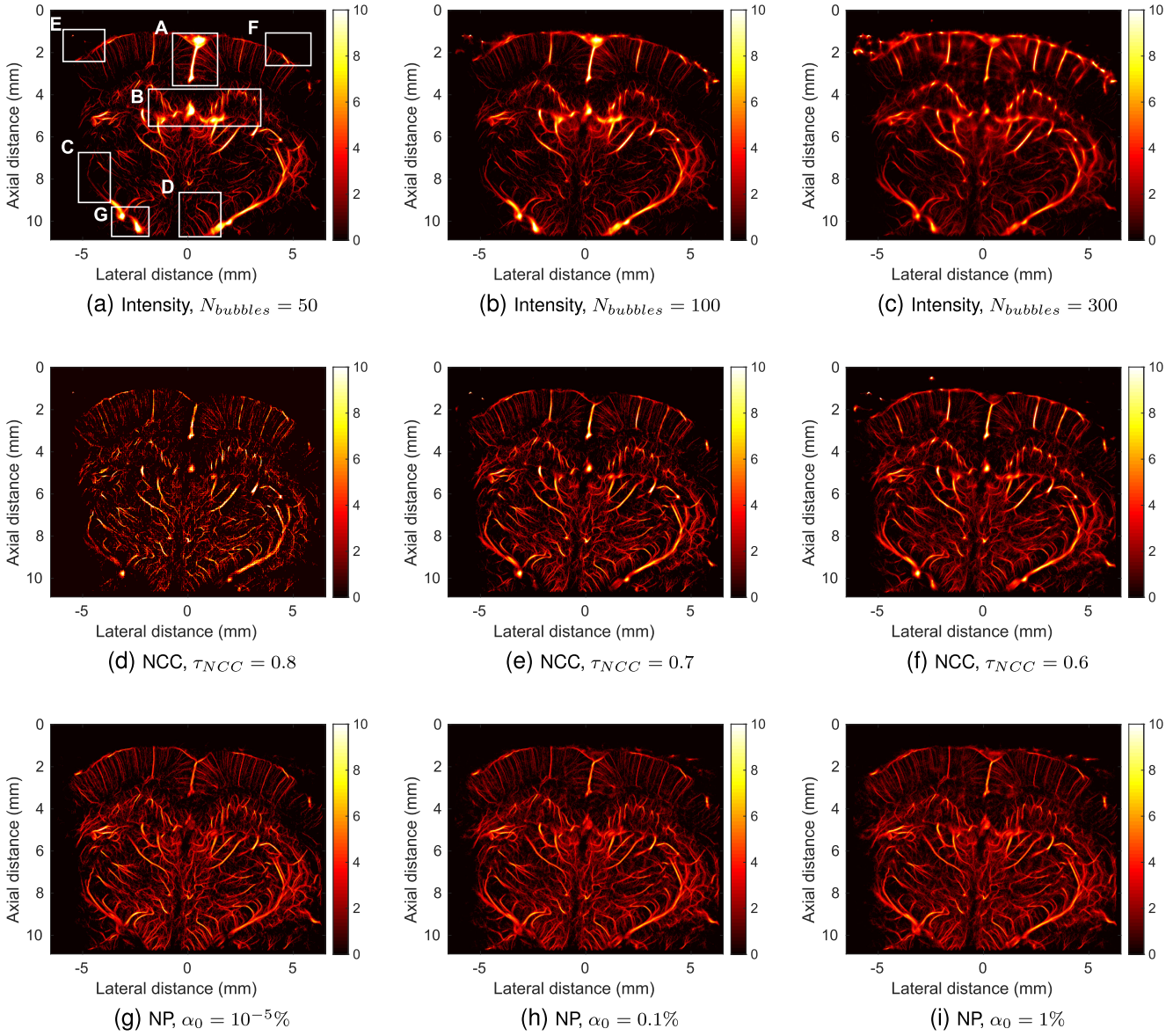

FIGURE 9. Density ULM images of rat brain in square root scale after histogram matching with (e). (a), (b), (c) with intensity-based detection respectively with $N_{bubbles}$ = 50, 100, 300. (d), (e), (f) with NCC detection respectively with τ_{NCC} = 0.8, 0.7, 0.6. (g), (h), (i) with Neyman–Pearson detection respectively with $\alpha_0 = 10^{-5}$%, 0.1%, 1%, acquisition time = 85.6 s.

α_0 parameter of $10^{-5}\%$, the NP detector is able to reconstruct a relatively complete map with a greater resolution compared to Fig. 9b but some bright structures (*e.g* areas A and G) are attenuated. By visualizing the data, one may note that these structures are large vessels with high MB concentration, so the pixels value over time are mainly composed of MB peaks and the noise parameter estimation fails since there are not enough noise samples in each pixel signal. Thus, the NP detector confuses the MBs in these vessels with noise and does not consider them in the detections. To recover them, α_0 can be increased to 0.1% as in Fig. 9h but at the expense of a few false alarm detections (area F). A higher false alarm rate of 1% in Fig. 9i induces more FP (area F) and artefacts (area A) but no significant detection of new vessels compared to Fig. 9g, h. This confirms the results of the simulation part, where the variation of α_0 induces mainly a variation on the FP detections. To conclude on the false alarm α_0 parameter, a constraining one as $10^{-5}\%$ provides an exploitable map since most of the vessels are represented. If one is interested in the vessels perpendicular to the imaging plane, a higher but reasonable α_0 has to be chosen, for example 0.1%.

Concerning the intensity-based detector, the highest-density areas seem to be related to the highest MB intensities visible in Fig. 4, which is an undesirable effect of this detector. This can be explained by the fact that structures with the highest intensity are detected first when using the intensity-based detector, including MBs and undesired residual tissue. Since the number of structures to be detected is limited by the user, some MBs darker than residual artifacts are missed by this detector. This effect is removed with the NCC and NP

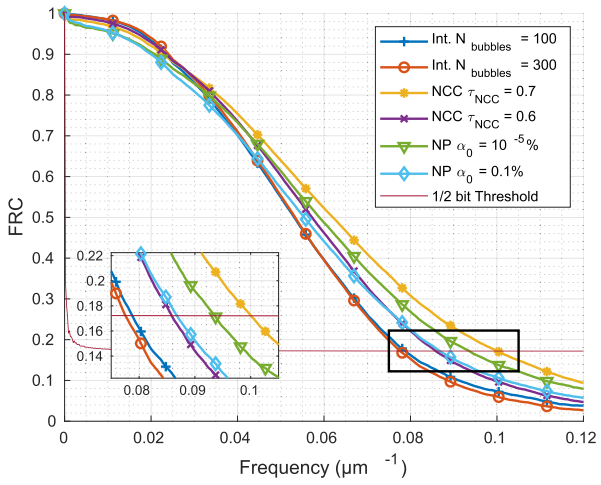

FIGURE 10. **Fourier-ring correlation curves for all methods.**

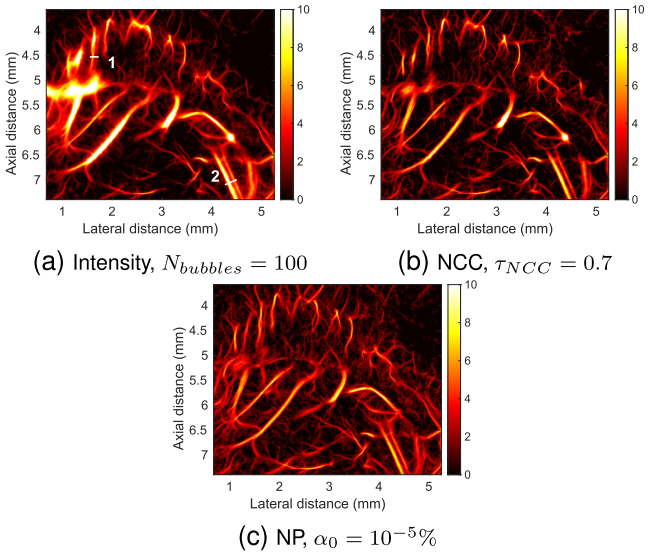

FIGURE 11. **Zoom on density ULM images of rat brain (a) with intensity-based detection $N_{bubbles} = 100$, (b) with NCC detection $\tau_{NCC} = 0.7$, (c) with Neyman–Pearson detection, $\alpha_0 = 10^{-5}\%$. The scale is in square root after histogram matching with Fig. 9e.**

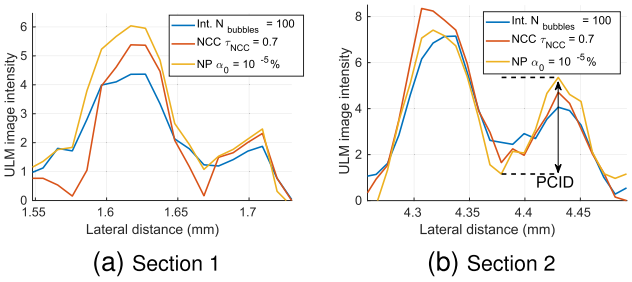

FIGURE 12. **Sections values for each detection methods and PCID illustration.**

detector, as shown in Fig. 9e, g where the density is more spatially uniform.

To compare quantitatively the detection methods, results are given through the Fourier-ring correlation (FRC) [20]. This metric allows us to measure the resolution of an image in ULM by means of the 2D Fourier transform, which gives information on the frequencies in the image. An image with high frequencies means that closely situated structures can be identified and thus the resolution is good. This metric is non-sensitive to noise since the Fourier transform is performed on two subsets of the tracks and a cross-correlation is made to remove the noise impact. The results of the FRC applied to the whole image are displayed in Fig. 10. The significant frequencies are defined by the intersection between the FRC curves and the $1/2$ bit threshold and the resolution is obtained by the inverse of these frequencies. Independently of the method, a less constraining parameter leads to a loss of resolution. For the intensity method the best resolution is 12.8μm, 10μm for the NCC, and 10.6μm for the NP detection. Thus, the NCC and the NP detection yields the best resolutions, specifically with the lower τ_{NCC} and α_0, which leads to a gain in resolution of 22% and 17% respectively compared with the intensity-based method with $N_{bubbles} = 100$. This resolution gain is illustrated with the example in Fig. 11, where two sections (white lines marked 1 and 2) are represented on Fig. 11b. These sections are perpendicular to two close parallel vessels and are shown in Fig. 12. The metric used on these sections is the peak to center intensity difference (PCID) [51]. An example of PCID with the NCC results is represented on Fig. 12a. For the section I, the PCID are 0.70, 2.15 and 1.40 respectively for the intensity-based, NCC and NP detection methods. For the second section in Fig. 12b, the PCID for these methods in the same order are 1.65, 3.10 and 4.20. It is clear that the NCC and NP methods provide higher PCID metrics in these two examples and thus justifies the higher resolution indicated by the FRC.

The results above demonstrated that NCC and NP methods had close performances in terms of resolution, and better than the intensity-based method. However, it has been discussed by analysing the Fig. 9e, f that the NCC method was not able to connect vessels between them in some cases, as it is highlighted in Fig. 13b. To fully connect the vessels as in Fig. 13a, the parameter τ_{NCC} needs to be decreased to 0.5, but this implies disturbing artefacts (Fig. 13c). This means that in the area where vessels are connected, the PSF does not have a Gaussian shape. This can be due to phase aberration or overlapping MBs in this specific areas that distorts the PSF shape. This observation shows the limits of the NCC detection method that is sensitive to PSF shape, while in the context of ULM, this shape is a function of time and space [52]. Meanwhile, the NP method is able to connect the vessels as it can be seen in Fig. 13d.

Finally, the benefit of spatially uniform detection is highlighted in Fig. 14, which is a vessel map built from 4-s acquisitions. Instead of detecting only the brightest MBs and drawing redundant stuctures, NCC and NP detections allow the density map to be filled faster with vessels (*e.g.* in areas C and D), as shown in Fig. 14b and Fig. 14c compared to Fig. 14a. Even if some structures in Fig. 14c. are not as bright as in Fig. 14b, they are, nevertheless, represented. This is

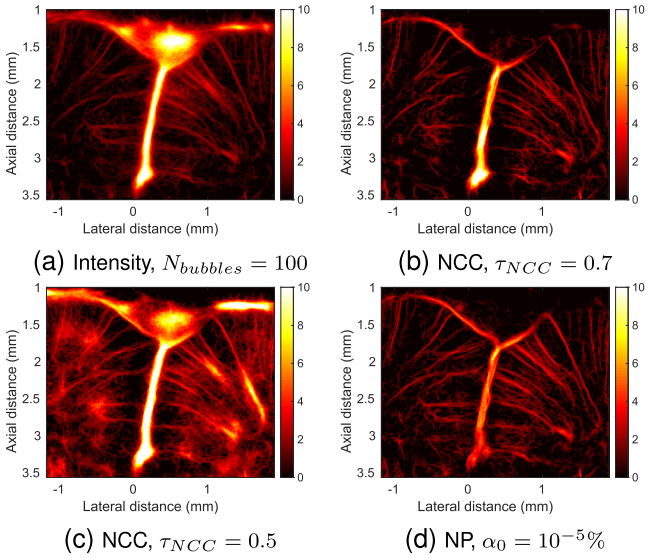

FIGURE 13. Zoom on density ULM images of rat brain (a) with intensity-based detection $N_{bubbles}$ = 100, (b) and (c) with NCC detection τ_{NCC} = 0.7 and 0.5, (d) with Neyman–Pearson detection, $\alpha_0 = 10^{-5}$%. The scale is in square root after histogram matching with Fig. 9e.

important regarding the definition of the saturation metric, which counts the number of non-null pixels for a given time. However, this metric is highly sensitive to noise, so only a qualitative saturation is studied in the paper. In this example with a very short acquisition time, a low τ_{NCC} and a relatively high α_0 of 1% are chosen to maximize the number of detected MBs. The parameter $N_{bubbles}$ for the intensity method is kept unchanged to avoid resolution issues.

E. RESULTS FROM IN VIVO RAT KIDNEY DATA

In order to complete the study, the methods are evaluated on a rat kidney *in vivo* dataset. First, the spatially uniform detection benefits are clear in this example as it can be seen by comparing Fig. 15a with Fig. 15d, f. The densities are more uniform with the NCC and NP detection methods with well chosen threshold parameters. Indeed, there are fewer tracks for large vessels but more details for small vessels in areas B and C. To detect these small vessels with the intensity-based method, the parameter $N_{bubbles}$ needs to be increased as in Fig. 15b. However, instead of detecting the vessels in these areas, it detects more FP in the circular areas and in area D. Note that only the NP method removes these punctual FP detections.

From visual inspection of the results in Fig. 15a, d, f, one may note that there is not significant difference in spatial resolution between the different methods. This is confirmed by the resolutions indicated by the FRC values equal to 35μm for all methods, except for the NCC with $\tau_{NCC} = 0.6$ for which the resolution is equal to 31.25μm. Note however that in Fig. 15d, some strong and local artefacts appear in the circular areas, which may induce a bias in the resolution indicated by the FRC according to [20]. Therefore, this makes the resolution analysis difficult in this particular case.

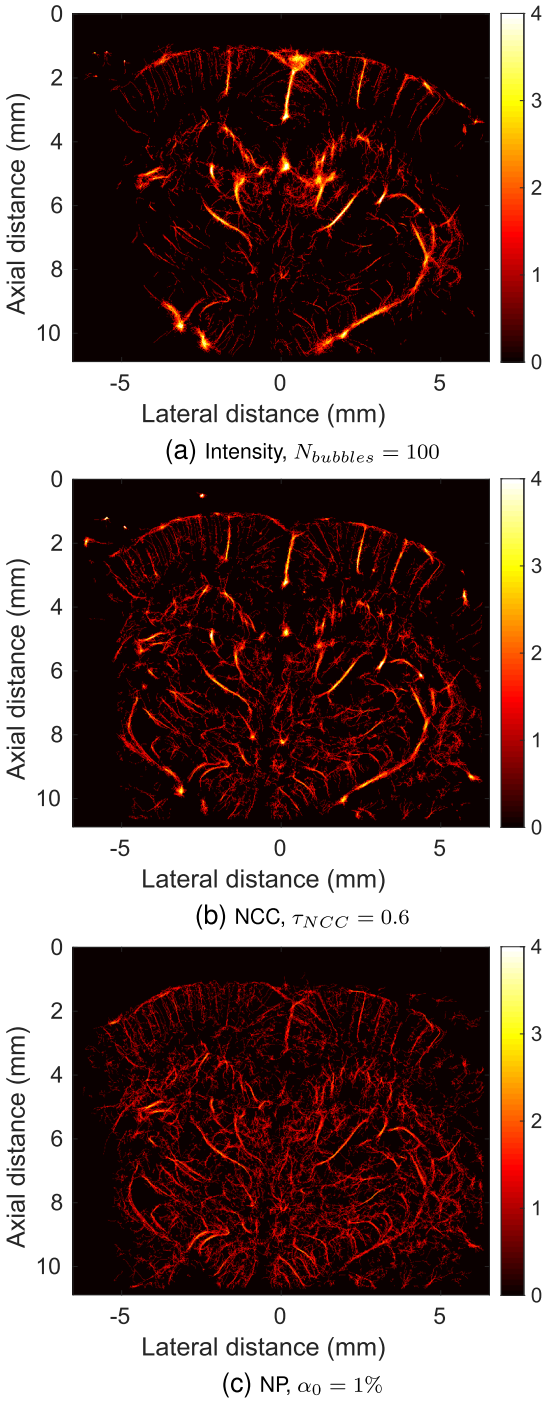

FIGURE 14. Density ULM images of rat brain (a) with intensity-based detection $N_{bubbles}$ = 100, (b) with NCC detection τ_{NCC} = 0.6, (c) with Neyman–Pearson detection α_0 = 1%, acquisition time = 4 s. The scale is in square root after histogram matching with (b).

In Fig. 15c, e, the NCC and NP methods are challenged by choosing a threshold too restrictive to study their risks. In both figures, the wide vessel in area A is eroded but for different reasons. For the NCC method, the reason is that the PSFs shapes in this area are not similar to a Gaussian shape as it can be seen in Fig. 5. This is explained by the

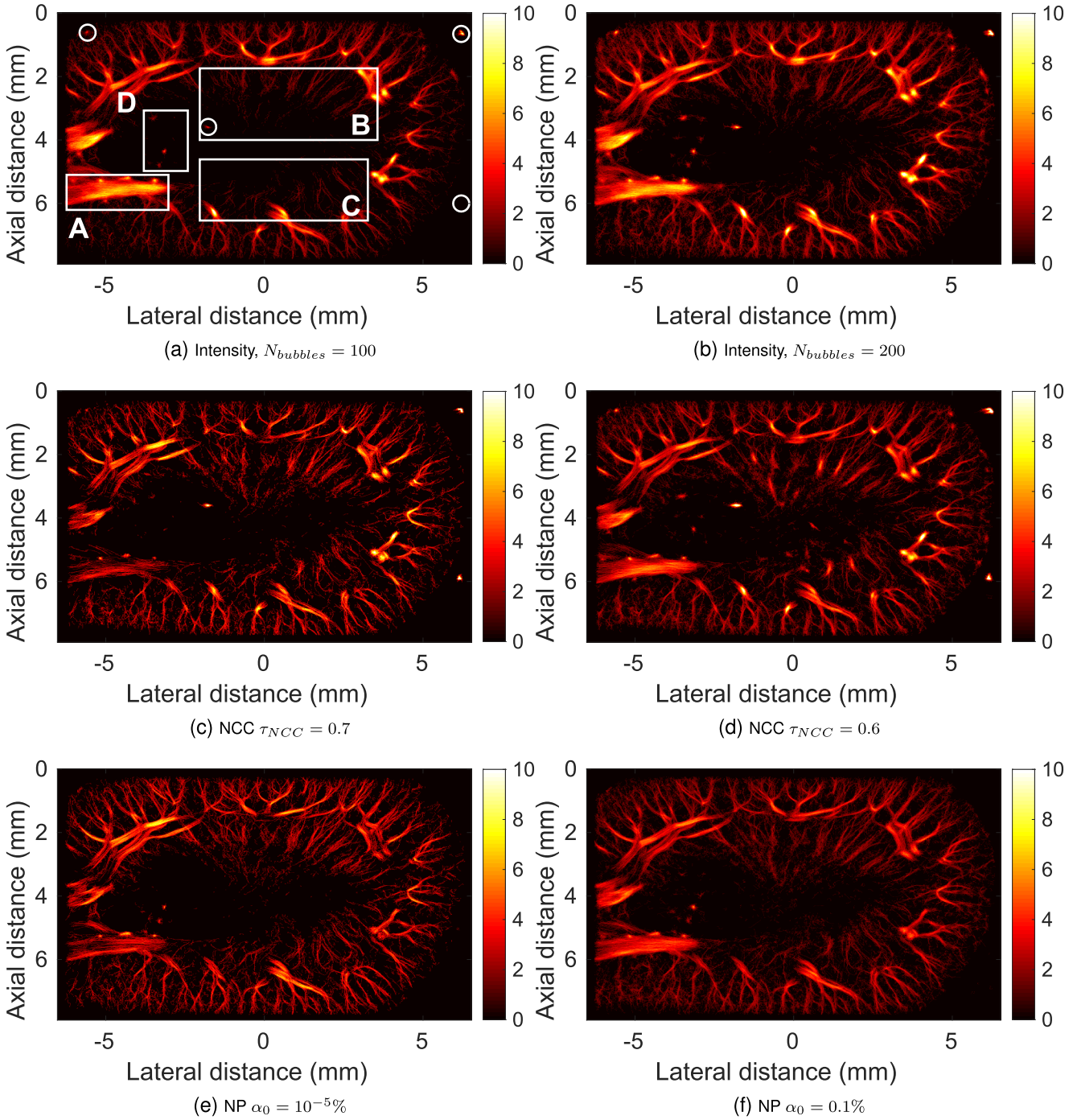

FIGURE 15. Density ULM images of rat kidney in square root scale after histogram matching with (a), (a), (b) with intensity-based detection $N_{bubbles} = 100$ and $N_{bubbles} = 200$, (c), (d) with NCC detection, $\tau_{NCC} = 0.7$ and $\tau_{NCC} = 0.6$, (e), (f) with Neyman–Pearson detection $\alpha_0 = 10^{-5}\%$ and $\alpha_0 = 1\%$, acquisition time = 94 s.

high MBs concentration in this vessel, resulting into the super-position of several overlapping PSFs. Thus, these PSFs are flat, extended in the lateral direction while an isolated MB, *e.g.* at coordinates (-4mm, 2mm) for the lateral and axial axis, is more similar to a Gaussian. Consequently, for a too constraining parameter, the NCC is sensitive to PSF shape alterations. Moreover, for the NP detection method, the reason is also linked to the high MB concentration, but differs mathematically. We remind the illustration in Fig. 2b with the signal peaks due to MBs passages. In the case of an excessive number of signal peaks, *i.e.* an excessive number of MBs passages, which occurs in the case of high MB concentration, the NP method risks to confuse the MB peaks and the noise since the pixel signal over time is mainly composed of MB peaks and therefore the method has not enough noise samples to estimate the noise mean and standard deviation

following (16) and (17). That is why for both NCC and NP methods, in a context of local high MB concentration, the threshold parameter must be set to a reasonable value.

V. CONCLUSION AND PERSPECTIVES

In this paper, an MB detector based on the Neyman–Pearson criterion is proposed and compared with the intensity-based and the normalized cross-correlation detectors. We show through simulation and *in vivo* study that the new detector makes it possible to control easily the false positive detections without overly deteriorating the true positive ones.

It has been shown that the intensity-based detection method is sensitive to noise. Therefore, vessels with low intensity are difficult to detect, because of MBs moving similar to residual tissue. This trade-off is limited with the NCC and NP methods. In addition to that, these methods provide significant benefits for ULM:

- detecting MBs with intensity lower than noise and residual tissue,
- enhancing the resolution,
- detecting MBs in a more spatially uniform way and provide a more complete map for an equivalent acquisition time.

However, the NCC-based detector is limited in the case where the shape of the PSFs varies as a function of space. These variations can be induced by phase aberrations or PSF overlapping in vessels with high MB concentration. This leads to a partial vessel reconstruction but can be corrected without adding excessive noise by adjusting the τ_{NCC} threshold. This can also generate some disconnections in vessel junctions, which is harder to correct by adjusting the τ_{NCC} parameter.

The NP method presents also a risk of partial vessel reconstruction for high MB concentration in a vessel. If the MBs cross a pixel too frequently, the algorithm can confuse the MBs and the noise. This can easily be corrected by increasing the α_0 parameter without adding disturbing noise.

It would be interesting to evaluate this new tool in cases where the bubble response is low, and particularly if the ULM is not applied to bubbles but to red blood cells as done in [53]. Moreover, this detector has a low calculation cost, and therefore it can easily be adaptable to 3D ULM.

A further study would be to evaluate a different statistical distribution for noise and MB intensity in Eq. (4), for example, by assuming that the MB intensity follows a Gaussian law. However, with this hypothesis, the value B will not be simplified in the calculus and it will introduce new parameters to be estimated as the mean and standard deviation of the MB intensity distribution. It could also be possible to deal with the decision theory problem without making any assumption on the MB signal distribution [43], [54].

NP DETECTION METHOD IMPLEMENTATION

The Matlab code for implementing the Neyman-Pearson detector is available on https://github.com/CorazzaAlexandre/Microbubble_detection.

ACKNOWLEDGMENT

The authors would like to thank the authors of the PALA toolbox for having made publicly available the ULM Matlab codes and ultrasound datasets.

REFERENCES

[1] C. Demené et al., "Transcranial ultrafast ultrasound localization microscopy of brain vasculature in patients," *Nature Biomed. Eng.*, vol. 5, no. 3, pp. 219–228, Mar. 2021, doi: 10.1038/s41551-021-00697-x.

[2] F. Lin, J. D. Rojas, and P. A. Dayton, "Super resolution contrast ultrasound imaging: Analysis of imaging resolution and application to imaging tumor angiogenesis," in *Proc. IEEE Int. Ultrason. Symp. (IUS)*, Sep. 2016, pp. 1–4.

[3] F. Lin, S. E. Shelton, D. Espíndola, J. D. Rojas, G. Pinton, and P. A. Dayton, "3-D ultrasound localization microscopy for identifying microvascular morphology features of tumor angiogenesis at a resolution beyond the diffraction limit of conventional ultrasound," *Theranostics*, vol. 7, no. 1, pp. 196–204, 2017.

[4] D. Fukumura, D. G. Duda, L. L. Munn, and R. K. Jain, "Tumor microvasculature and microenvironment: Novel insights through intravital imaging in pre-clinical models," *Microcirculation*, vol. 17, no. 3, pp. 206–225, Apr. 2010, doi: 10.1111/j.1549-8719.2010.00029.x.

[5] F. Yuan, H. A. Salehi, Y. Boucher, U. S. Vasthare, R. F. Tuma, and R. K. Jain, "Vascular permeability and microcirculation of gliomas and mammary carcinomas transplanted in rat and mouse cranial windows1," *Cancer Res.*, vol. 54, no. 17, pp. 4564–4568, Sep. 1994.

[6] D. M. McDonald and P. L. Choyke, "Imaging of angiogenesis: From microscope to clinic," *Nature Med.*, vol. 9, no. 6, pp. 713–725, Jun. 2003.

[7] T. Opacic et al., "Motion model ultrasound localization microscopy for preclinical and clinical multiparametric tumor characterization," *Nature Commun.*, vol. 9, no. 1, pp. 1–10, Apr. 2018.

[8] D. Ghosh, F. Xiong, R. Mattrey, S. Sirsi, and K. Hoyt, "Monitoring early tumor response to vascular targeted therapy using super-resolution ultrasound imaging," in *Proc. IEEE Int. Ultrason. Symp. (IUS)*, Sep. 2017, p. 1.

[9] V. Perrot, M. Polichetti, F. Varray, and D. Garcia, "So you think you can DAS? A viewpoint on delay-and-sum beamforming," *Ultrasonics*, vol. 111, Jan. 2021, Art. no. 106309. [Online]. Available: https://www.sciencedirect.com/science/article/pii/S0041624X20302444

[10] O. Couture, V. Hingot, B. Heiles, P. Muleki-Seya, and M. Tanter, "Ultrasound localization microscopy and super-resolution: A state of the art," *IEEE Trans. Ultrason., Ferroelectr., Freq. Control*, vol. 65, no. 8, pp. 1304–1320, Aug. 2018. [Online]. Available: https://hal.archives-ouvertes.fr/hal-02344318

[11] K. Christensen-Jeffries et al., "Super-resolution ultrasound imaging," *Ultrasound Med. Biol.*, vol. 46, no. 4, pp. 865–891, 2020. [Online]. Available: https://www.sciencedirect.com/science/article/pii/S0301562919315959

[12] B. Heiles, A. Chavignon, V. Hingot, P. Lopez, E. Teston, and O. Couture, "Performance benchmarking of microbubble-localization algorithms for ultrasound localization microscopy," *Nature Biomed. Eng.*, vol. 6, no. 5, pp. 605–616, Feb. 2022, doi: 10.1038/s41551-021-00824-8.

[13] C. Demené et al., "Spatiotemporal clutter filtering of ultrafast ultrasound data highly increases Doppler and fUltrasound sensitivity," *IEEE Trans. Med. Imag.*, vol. 34, no. 11, pp. 2271–2285, Nov. 2015.

[14] J. Baranger, B. Arnal, F. Perren, O. Baud, M. Tanter, and C. Demené, "Adaptive spatiotemporal SVD clutter filtering for ultrafast Doppler imaging using similarity of spatial singular vectors," *IEEE Trans. Med. Imag.*, vol. 37, no. 7, pp. 1574–1586, Jul. 2018.

[15] M. A. O'Reilly and K. Hynynen, "A super-resolution ultrasound method for brain vascular mapping," *Med. Phys.*, vol. 40, no. 11, pp. 1–7, Nov. 2013.

[16] D. Ackermann and G. Schmitz, "Detection and tracking of multiple microbubbles in ultrasound B-mode images," *IEEE Trans. Ultrason., Ferroelectr., Freq. Control*, vol. 63, no. 1, pp. 72–82, Jan. 2016.

[17] C. Bourquin, J. Porée, F. Lesage, and J. Provost, "In vivo pulsatility measurement of cerebral microcirculation in rodents using dynamic ultrasound localization microscopy," *IEEE Trans. Med. Imag.*, vol. 41, no. 4, pp. 782–792, Apr. 2022.

[18] P. Song et al., "Improved super-resolution ultrasound microvessel imaging with spatiotemporal nonlocal means filtering and bipartite graph-based microbubble tracking," *IEEE Trans. Ultrason., Ferroelectr., Freq. Control*, vol. 65, no. 2, pp. 149–167, Feb. 2018.
[19] Y. Desailly, O. Couture, M. Fink, and M. Tanter, "Sono-activated ultrasound localization microscopy," *Appl. Phys. Lett.*, vol. 103, no. 17, Oct. 2013, Art. no. 174107, doi: 10.1063/1.4826597.
[20] V. Hingot, A. Chavignon, B. Heiles, and O. Couture, "Measuring image resolution in ultrasound localization microscopy," *IEEE Trans. Med. Imag.*, vol. 40, no. 12, pp. 3812–3819, Dec. 2021.
[21] O. Couture, B. Besson, G. Montaldo, M. Fink, and M. Tanter, "Microbubble ultrasound super-localization imaging (MUSLI)," in *Proc. IEEE Int. Ultrason. Symp.*, Oct. 2011, pp. 1285–1287.
[22] P. Song, A. Manduca, J. D. Trzasko, R. E. Daigle, and S. Chen, "On the effects of spatial sampling quantization in super-resolution ultrasound microvessel imaging," *IEEE Trans. Ultrason., Ferroelectr., Freq. Control*, vol. 65, no. 12, pp. 2264–2276, Dec. 2018.
[23] R. Henriques, M. Lelek, E. F. Fornasiero, F. Valtorta, C. Zimmer, and M. M. Mhlanga, "QuickPALM: 3D real-time photoactivation nanoscopy image processing in ImageJ," *Nature Methods*, vol. 7, no. 5, pp. 339–340, May 2010, doi: 10.1038/nmeth0510-339.
[24] R. Parthasarathy, "Rapid, accurate particle tracking by calculation of radial symmetry centers," *Nature Methods*, vol. 9, no. 7, pp. 724–726, Jul. 2012.
[25] C. Errico et al., "Ultrafast ultrasound localization microscopy for deep super-resolution vascular imaging," *Nature*, vol. 527, no. 7579, pp. 499–502, Nov. 2015, doi: 10.1038/nature16066.
[26] H. W. Kuhn, *The Hungarian Method for the Assignment Problem*. Berlin, Germany: Springer, 2010, pp. 29–47, doi: 10.1007/978-3-540-68279-0_2.
[27] S. Oh, S. Russell, and S. Sastry, "Markov chain Monte Carlo data association for multi-target tracking," *IEEE Trans. Autom. Control*, vol. 54, no. 3, pp. 481–497, Mar. 2009.
[28] G. A. Brock-Fisher, "Means for increasing sensitivity in non-linear ultrasound imaging systems," *J. Acoust. Soc. Amer.*, vol. 101, no. 6, p. 3240, Jun. 1997.
[29] D. H. Simpson, C. T. Chin, and P. N. Burns, "Pulse inversion Doppler: A new method for detecting nonlinear echoes from microbubble contrast agents," *IEEE Trans. Ultrason., Ferroelectr., Freq. Control*, vol. 46, no. 2, pp. 372–382, Mar. 1999.
[30] K. Brown and K. Hoyt, "Simultaneous evalulation of contrast pulse sequences for super-resolution ultrasound imaging—Preliminary in vitro and in vivo results," in *Proc. 42nd Annu. Int. Conf. IEEE Eng. Med. Biol. Soc. (EMBC)*, Jul. 2020, pp. 2121–2124.
[31] E. J. Candès, X. Li, Y. Ma, and J. Wright, "Robust principal component analysis?" *J. ACM*, vol. 58, no. 3, pp. 1–12, 2011.
[32] K. Xu et al., "Robust PCA-based clutter filtering method for super-resolution ultrasound localization microscopy," in *Proc. IEEE Int. Ultrason. Symp. (IUS)*, Sep. 2021, pp. 1–4.
[33] C. Huang et al., "Short acquisition time super-resolution ultrasound microvessel imaging via microbubble separation," *Sci. Rep.*, vol. 10, no. 1, pp. 1–13, Apr. 2020.
[34] Y. Deville, *Signaux Temporels et Spatiotemporels: Analyse des Signaux, théorie de Information, Traitement d'antenne, séparation Aveugle de Sources*. Paris, France: Ellipses, 2011.
[35] S. Tang et al., "Kalman filter-based microbubble tracking for robust super-resolution ultrasound microvessel imaging," *IEEE Trans. Ultrason., Ferroelectr., Freq. Control*, vol. 67, no. 9, pp. 1738–1751, Sep. 2020.
[36] J. Yan, T. Zhang, J. Broughton-Venner, P. Huang, and M. Tang, "Super-resolution ultrasound through sparsity-based deconvolution and multi-feature tracking," *IEEE Trans. Med. Imag.*, vol. 41, no. 8, pp. 1938–1947, Aug. 2022.
[37] Q. Chen, H. Song, J. Yu, and K. Kim, "Current development and applications of super-resolution ultrasound imaging," *Sensors*, vol. 21, no. 7, p. 2417, Apr. 2021. [Online]. Available: https://www.mdpi.com/1424-8220/21/7/2417
[38] R. J. G. van Sloun, O. Solomon, M. Bruce, Z. Z. Khaing, Y. C. Eldar, and M. Mischi, "Deep learning for super-resolution vascular ultrasound imaging," in *Proc. IEEE Int. Conf. Acoust., Speech Signal Process. (ICASSP)*, May 2019, pp. 1055–1059.
[39] J. Youn, M. L. Ommen, M. B. Stuart, E. V. Thomsen, N. B. Larsen, and J. A. Jensen, "Detection and localization of ultrasound scatterers using convolutional neural networks," *IEEE Trans. Med. Imag.*, vol. 39, no. 12, pp. 3855–3867, Dec. 2020.
[40] X. Liu, T. Zhou, M. Lu, Y. Yang, Q. He, and J. Luo, "Deep learning for ultrasound localization microscopy," *IEEE Trans. Med. Imag.*, vol. 39, no. 10, pp. 3064–3078, Oct. 2020.
[41] J. Brown et al., "Investigation of microbubble detection methods for super-resolution imaging of microvasculature," *IEEE Trans. Ultrason., Ferroelectr., Freq. Control*, vol. 66, no. 4, pp. 676–691, Apr. 2019.
[42] C. L. Weber, *Radar Detection Theory*. New York, NY, USA: Springer, 1987, pp. 45–51, doi: 10.1007/978-1-4612-4774-6_6.
[43] E. Conte, A. De Maio, and C. Galdi, "Signal detection in compound-Gaussian noise: Neyman–Pearson and CFAR detectors," *IEEE Trans. Signal Process.*, vol. 48, no. 2, pp. 419–428, Apr. 2000.
[44] D. Garcia, "SIMUS: An open-source simulator for medical ultrasound imaging. Part I: Theory & examples," *Comput. Methods Programs Biomed.*, vol. 218, May 2022, Art. no. 106726.
[45] K. Christensen-Jeffries et al., "Microbubble axial localization errors in ultrasound super-resolution imaging," *IEEE Trans. Ultrason., Ferroelectr., Freq. Control*, vol. 64, no. 11, pp. 1644–1654, Nov. 2017.
[46] D. Declercq and A. Quinquis, *Détection et Estimation des Signaux* (Traitement du Signal). Paris, France: Hermès, 1996.
[47] S. O. Hansson, *Decision Theory: An Overview*. Berlin, Germany: Springer, 2011, pp. 349–355, doi: 10.1007/978-3-642-04898-2_22.
[48] T. Pham-Gia and T. L. Hung, "The mean and median absolute deviations," *Math. Comput. Model.*, vol. 34, nos. 7–8, pp. 921–936, Oct. 2001.
[49] O. Michailovich and Y. Rathi, "Adaptive learning of tissue reflectivity statistics and its application to deconvolution of medical ultrasound scans," in *Proc. IEEE Int. Ultrason. Symp. (IUS)*, Oct. 2015, pp. 1–4.
[50] N. Bottenus, B. C. Byram, and D. Hyun, "Histogram matching for visual ultrasound image comparison," *IEEE Trans. Ultrason., Ferroelectr., Freq. Control*, vol. 68, no. 5, pp. 1487–1495, May 2021.
[51] C. Fan, M. Caleap, M. Pan, and B. W. Drinkwater, "A comparison between ultrasonic array beamforming and super resolution imaging algorithms for non-destructive evaluation," *Ultrasonics*, vol. 54, no. 7, pp. 1842–1850, Sep. 2014. [Online]. Available: https://www.sciencedirect.com/science/article/pii/S0041624X13003661
[52] M. I. Florea, A. Basarab, D. Kouame, and S. A. Vorobyov, "Restoration of ultrasound images using spatially-variant kernel deconvolution," in *Proc. IEEE Int. Conf. Acoust., Speech Signal Process. (ICASSP)*, Apr. 2018, pp. 796–800.
[53] J. A. Jensen et al., "Fast super resolution ultrasound imaging using the erythrocytes," *Proc. SPIE*, vol. 12038, pp. 79–84, Jan. 2022, doi: 10.1117/12.2612245.
[54] D. Pastor, "Two results in statistical decision theory for detecting signals with unknown distributions and priors in white Gaussian noise," in *Proc. Int. Symp. Appl. Stochastic Models Data Anal.*, Brest, France, May 2005, p. 5. [Online]. Available: https://hal.archives-ouvertes.fr/hal-02137176